Structure and magnetism in $Sr_{1-x}A_xTcO_3$ perovskites: Importance of the *A*-site cation

Emily Reynolds
Inorganic Chemistry Laboratory, University of Oxford, South Parks Road, Oxford OX1 3QR, United Kingdom

Maxim Avdeev and Gordon J. Thorogood
Australian Nuclear Science and Technology Organisation, Lucas Heights, NSW 2234, Australia

Frederic Poineau and Kenneth R. Czerwinski
Department of Chemistry and Biochemistry, University of Nevada Las Vegas, 4505 Maryland Parkway, Las Vegas, Nevada 89154, USA

Justin A. Kimpton
Australian Synchrotron, 800 Blackburn Road, Clayton, Victoria 3168, Australia

Michelle Yu, Paula Kayser, and Brendan J. Kennedy
School of Chemistry, The University of Sydney, Sydney, NSW 2006, Australia
(Received 22 August 2016; revised manuscript received 10 January 2017; published 27 February 2017)

The $Sr_{1-x}Ba_xTcO_3$ ($x = 0, 0.1, 0.2$) oxides were prepared and their solid-state and magnetic structure studied as a function of temperature by x-ray and neutron powder diffraction. The refined Tc moments at room temperature and Néel temperatures for $Ba_{0.1}Sr_{0.9}TcO_3$ and $Ba_{0.2}Sr_{0.8}TcO_3$ were 2.32(14) μ_β and 2.11(13) μ_β and 714 °C and 702 °C, respectively. In contrast to expectations, the Néel temperature in the series $Sr_{1-x}A_xTcO_3$ decreases with increasing Ba content. This observation is consistent with previous experimental measurements for the two series AMO_3 (M = Ru, Mn; A = Ca, Sr, Ba) where the maximum magnetic ordering temperature was observed for A = Sr. Taken with these previous results the current work demonstrates the critical role of the *A*-site cation in the broadening of the π^* bandwidth and ultimately the magnetic ordering temperature.

DOI: 10.1103/PhysRevB.95.054430

I. INTRODUCTION

Strontium technetate, $SrTcO_3$, has emerged as an important case study in understanding the condensed matter science of 4*d* and 5*d* metal oxides [1–4]. At room temperature it, like its lighter Mn analog $SrMnO_3$, exhibits a *G*-type antiferromagnetic arrangement [4,5]. Both structures are built on corner-sharing MO_6 octahedra, although cooperative tilting of the octahedra lowers the symmetry in $SrTcO_3$ [6] to the orthorhombic $GdFeO_3$-type structure. While $SrMnO_3$ (Mn^{4+} $3d^4$) has an unexceptional Néel temperature ($T_N \sim$ 233 K), the Néel temperature in $SrTcO_3$ (Tc^{4+} $4d^3$) is exceptionally high, $T_N \sim 1000$ K [4]. Remarkably, the magnetic moment of the Tc ($\sim$2.1 μ_β at 3 K) is smaller than that seen at the same temperature in $SrMnO_3$ $\sim$ 2.6 μ_β [5]. Strontium ruthenate, $SrRuO_3$ (Ru^{4+} $4d^4$), is isostructural with $SrTcO_3$ but is ferromagnetic with a Curie temperature (T_C) of $\sim$160 K [7,8]. The $5d^3$ oxide $NaOsO_3$ is a Curie-Weiss metal at high temperature and transforms to an antiferromagnetically insulating state on cooling to 410 K [9]. The large observed variation in electronic properties is a consequence of the nature of the 4*d* and 5*d* orbitals, which are more extended than that of the 3*d*, resulting in a delicate balance between localized and correlated *d* electrons.

Prior to the discovery of antiferromagnetism (AFM) persisting to very high temperatures in $SrTcO_3$ ($T_N \sim 1000$ K) [4] and $CaTcO_3$ ($T_N \sim 800$ K) [10], it was generally accepted that the more extended 4*d* and 5*d* orbitals tended not to support strong magnetic exchange, relative to the 3*d* oxides. It is now understood that strong hybridization between metal 4*d* and O 2*p* states, when the t_{2g} orbitals are half filled $(t_{2g})^3(e_g)^0$, results in strong covalence of the Tc-O interaction which in turn results in exceptionally strong magnetic exchange parameters [11].

A challenge in the study of the fascinating magnetic properties of $SrTcO_3$ is that all known isotopes of Tc are radioactive; this limits the number of experimentally well studied Tc oxides that can be used to benchmark the numerous theoretical studies [3,12–16]. The unique physical properties of $SrTcO_3$, however, justify overcoming the challenges of working with radioactive material. One approach to furthering our understanding of the origin of the high Néel temperature in $SrTcO_3$ is to experimentally study the effect of *A*-site doping on the magnetic properties. Structurally, $CaTcO_3$ is more distorted than $SrTcO_3$, reflecting the smaller size of the Ca^{2+} cation relative to Sr^{2+}. Distortion of the TcO_6 octahedra, together with a decrease in the Tc-O-Tc bond angle, is expected to reduce the 4*d* bandwidth and suppress the kinetic energy gain relative to the formation of the magnetic states. This can explain the higher Néel temperature in $SrTcO_3$ compared to $CaTcO_3$.

Calculations have predicted [11,17] that $BaTcO_3$ would have a yet higher Néel temperature, as the larger Ba^{2+} cation will favor an even less distorted structure and larger Tc-O-Tc bond angle, and hence a stronger superexchange interaction. Considering that the perovskite tolerance factor t of $BaTcO_3$ is greater than 1, it is possible that the stable structure of $BaTcO_3$ may be cubic or hexagonal; a similar phenomenon has been observed for $SrMnO_3$ ($t = 1.04$) [18]. Indeed the very limited literature indicates that, when formed at ambient pressure, $BaTcO_3$ adopts an edge-sharing hexagonal [19]. Nevertheless, exploring the structure and magnetic properties of the series

$Sr_{1-x}A_xTcO_3$ (A = Ca, Ba) provides a means to establishing if tuning the $SrTcO_3$ structure by A-site doping allows the Néel temperature to be increased over that seen for $SrTcO_3$. In the present work, we establish how much Ba can be incorporated into the orthorhombic $SrTcO_3$ structure. The resulting samples have been characterized using synchrotron x-ray diffraction (SXRD), Tc K-edge x-ray absorption spectroscopy and, in selected cases, their magnetic ordering temperature established using neutron powder diffraction (NPD).

II. RESULTS

A. Experiment

Caution! ^{99}Tc is a β emitter ($E_{max} = 0.29$ MeV). All manipulations were performed in a laboratory designed for radioactivity using efficient HEPA-filtered fume hoods, and following locally approved radiochemistry handling and monitoring procedures. Laboratory coats, disposable gloves, and protective eyewear were worn at all times.

The $Sr_{1-x}Ba_xTcO_3$ ($x = 0, 0.1, 0.2, 0.3, 0.4$) oxides were prepared at UNLV by mixing and grinding stoichiometric amounts of $SrCO_3$, $BaCO_3$, and TcO_2. The resulting mixtures were placed in a quartz boat and treated at 900 °C for 45 h under flowing argon. Intermittent regrindings were performed in order to optimize the formation of a single-phase sample. The resulting black powders were initially characterized using laboratory powder x-ray diffraction (PXRD). Such measurements established that the maximum Ba content the structure could accommodate under these conditions was 40%. Attempts at the synthesis of $Ba_{0.5}Sr_{0.5}TcO_3$ were unsuccessful, and resulted in the formation of separate Ba and Sr technetate phases (see Supplemental Material (SM) [20]). It is possible that alternate synthetic methods, such as high pressure or sol-gel, may extend the range extent of Ba doping in the series to above $x = 0.4$, and may reduce the extent of phase separation; however, it was not possible to explore these within our laboratories due to the radioactive nature of Tc.

The preparation of larger samples (~1.2–2 g) for neutron measurements was only achieved for $x = 0.1$ and 0.2 samples and for $Sr_{0.5}Ca_{0.5}TcO_3$. Attempted synthesis of larger samples with higher Ba compositions were unsuccessful with the conventional PXRD measurements showing evidence for bulk phase separation (see SM). Consequently, the $x = 0.1$ and $x = 0.2$ Ba-doped samples are the focus of this study. A single-phase sample of $Sr_{0.5}Ca_{0.5}TcO_3$ (~ 2 g) was prepared at ANSTO using the procedure described previously for $SrTcO_3$ [10]; this method did not yield single-phase $BaTcO_3$.

Synchrotron x-ray powder diffraction (SXRD) data were collected over the angular range $5° < 2\theta < 85°$, using x rays of wavelength 0.824 65 Å, on the powder diffractometer at the BL-10 beamline of the Australian Synchrotron [21]. The samples were housed in 0.2-mm-diameter capillaries that were rotated during the measurements. For neutron diffraction measurements the samples were sealed in 6-mm-diameter vanadium cans and neutron powder diffraction (NPD) data were obtained using the high-resolution powder diffractometer Echidna at ANSTO's OPAL facility at Lucas Heights [22]. The wavelengths of the incident neutrons, obtained using (335) and (331) reflections of a germanium monochromator, were 1.6220 and 2.4395 Å, respectively, as determined using data collected for a certified NIST SRM660b LaB_6 standard. This instrument has a maximum resolution of $\Delta d/d \sim 1 \times 10^{-3}$. X-ray absorption near-edge structure (XANES) spectra were collected at the Tc K-edge on beamline 12 at the Australian Synchrotron in transmission mode using argon-filled ionization chambers [23].

B. Crystal structures

Synchrotron XRD data were collected for the various $Sr_{1-x}A_xTcO_3$ oxides at room temperature. Examination of the SXRD profiles of the Ba-doped samples suggested these to be orthorhombic; however, there was no evidence for any M-point reflections that are diagnostic of in-phase tilting of the corner-sharing TcO_6 octahedra [24]. Under identical conditions we observed M-point reflections in the SXRD profiles of undoped $SrTcO_3$. Likewise there was no evidence for M-point reflections in the NPD pattern of the $Sr_{1-x}Ba_xTcO_3$ ($x = 0.1, 0.2$) samples, demonstrating the structures cannot be in *Pnma*. Attempts to fit the data for the four Ba-containing samples in the alternate orthorhombic space group *Imma*, which forms in $SrTcO_3$ upon heating [6], were unsuccessful. Scrutiny of the diffraction data indicated that the samples were actually a mixture of two phases. A model containing both an orthorhombic *Imma* and tetragonal $I4/mcm$ phase was developed and this provided a satisfactory fit to the SXRD data measured at room temperature; see Fig. 1.

Phase separation, involving coexistence of orthorhombic *Imma* and tetragonal $I4/mcm$ structures, has been observed in a number of perovskites including $SrTcO_3$ [6] and $SrRuO_3$ [25] upon heating and at room temperature in a number of solid solutions including complex manganites of the type $Sr_{1-x}Pr_xMnO_3$ [26] and in $BaPb_{1-x}Bi_xO_3$ at the superconducting composition [27]. It was established that each $Sr_{1-x}Ba_xTcO_3$ sample contains two phases of slightly different compositions, one with a higher than ideal Ba content and the

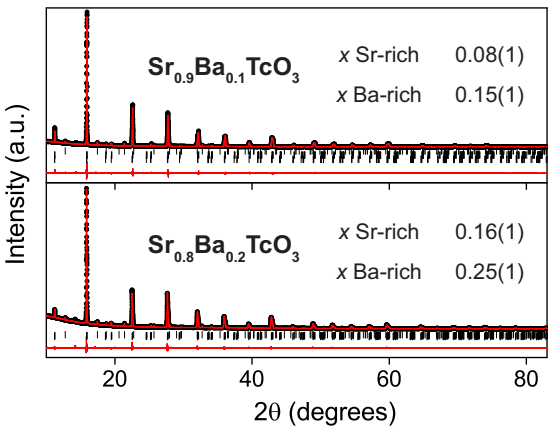

FIG. 1. Synchrotron diffraction profiles for $Sr_{0.9}Ba_{0.1}TcO_3$ and $Sr_{0.8}Ba_{0.2}TcO_3$ collected at room temperature. The symbols are the observed data and the solid line the calculated data. The difference between these is shown as a continuous line. There is an impurity Al_2O_3 phase from the mortar used for mixing the reactants. The refined compositions of the two phases (one Sr-rich and one Ba-rich, relative to the ideal composition) are shown above each data set.

TABLE I. Cation occupancy and phase abundance in the $Ba_xSr_{1-x}TcO_3$ samples established by Rietveld refinements against SXRD data. In all cases the lower-symmetry orthorhombic phase has a small volume and lower Ba content.

Ideal x	x in Sr-rich phase	Percent	Space group	Vol. (Å^3)	x in Ba-rich phase	Percent	Space group	Vol. (Å^3)
0.1	0.08(1)	80(1)	*Imma*	247.68	0.16(1)	20(1)	$I4/mcm$	250.28
0.2	0.15(1)	47(1)	*Imma*	247.76	0.25(1)	53(1)	$I4/mcm$	250.43
0.3	0.17(1)	73(1)	*Imma*	248.70	0.35(1)	27(1)	$I4/mcm$	250.63
0.4	0.19(1)	42(1)	*Imma*	249.78	0.45(1)	58(1)	$Pm3m$	251.30

other with a greater than ideal Sr content. Although the Ba content is less than 50% the former is Ba rich compared to the ideal composition. In each case the Ba-rich sample will have the larger tolerance factor and this leads to the stabilization of the tetragonal structure. The results of this analysis are summarized in Table I. The composition of two phases within each sample was established by refining the site occupancies against the SXRD data over a range of temperatures, including room temperature and in the high-temperature cubic region (see below). For each sample, the phase containing more Sr was observed to have a smaller cell volume, reflecting the difference in the size of the two cations, and lower symmetry. The latter reflects the smaller tolerance factors which are correlated with the introduction of cooperative tilting in perovskites. That the tetragonal structure exists in the $x = 0.1$ sample with a refined Ba content of 0.16(1) and a sample with effectively the same amount of Ba [0.15(1) in the $x = 0.2$ sample] has an orthorhombic structure represents both the limitations of Rietveld refinements to accurately and precisely establish this and the sensitivity of the transition. Table II gives the refined structural parameters for one example ($x = 0.2$). The SXRD profiles of the various Ba-doped samples were noticeably broader than that observed for $SrTcO_3$, suggesting the domains of the phase-separated compositions are relatively small. Further details are given in the Supplemental Material [20]. XAS measurements at the Tc K edge demonstrated the Tc to be tetravalent in all cases; see Fig. 2.

TABLE II. Refined structural parameters for $Ba_{0.2}Sr_{0.8}TcO_3$ from SXRD data recorded at room temperature, with $R_p = 0.033$ and $R_{wp} = 0.046$.

Composition	$Ba_{0.15}Sr_{0.85}TcO_3$	$Ba_{0.25}Sr_{0.75}TcO_3$
Space group	*Imma*	$I4/mcm$
Weight %	47.0(1)	53.0(1)
a (Å)	5.58517(8)	5.6146(7)
b (Å)	7.9067(2)	$= a$
c (Å)	5.605(2)	7.9443(3)
Ba/Sr	$4e$ $(0\ \frac{1}{4}\ z)$	$4b$ $(0\ ½\ \frac{1}{4})$
Z	0.498(2)	
B_{iso} (Å^2)	1.11(3)	1.03(2)
Tc	$4a$ (0 0 0)	$4c$ (0 0 0)
B_{iso} (Å^2)	0.39(2)	0.20(1)
O1	$4e$ $(0\ \frac{1}{4}\ z)$	$4a$ $(0\ 0\ \frac{1}{4})$
Z	0.046(4)	
B_{iso} (Å^2)	0.5(4)	0.8(7)
O2	$8g$ $(\frac{1}{4}\ y\ \frac{1}{4})$	$8h$ $(x\ x + \frac{1}{2}\ 0)$
x/y	0.511(3)	0.244(5)
B_{iso} (Å^2)	1.1(2)	0.7(4)

The temperature dependence of the structures was determined using SXRD. The appropriate space group was established through examination of the diagnostic splitting of the primitive perovskite reflections such as the $(222)_p$ and the nature of any superlattice reflections. For example, the evolution of the 112/211/031 multiplet showed that an $Imma \rightarrow I4/mcm$ transition occurred near 300 °C in the $x = 0.1$ sample. The 211 and 031 reflections overlap such that what is a single reflection (121) in the tetragonal structure appears as a doublet in the *Imma* orthorhombic structure. Once the appropriate space groups were established the structures were refined by the Rietveld method. The temperature dependence of the lattice parameters are shown in Fig. 3. Each sample undergoes the same sequence of phase transitions as observed for the $SrTcO_3$ end member [6], save none exhibited the *Pnma* structure observed for undoped $SrTcO_3$ at room temperature, $Imma(a^-a^-c^0) \rightarrow I4/mcm(a^0a^0c^-) \rightarrow Pm3m(a^0a^0a^0)$, where the corresponding Glazer tilt system is given in parentheses. This sequence of structures is a consequence of the systematic loss of the in-phase tilts of the corner-sharing TcO_6 octahedra upon heating and is frequently observed in perovskites [28]. The coexistence of the two phases was most easily observed by examination of the high-temperature SXRD profiles where both phases adopted a cubic structure (see SM [20]).

C. Magnetic structures

Since it was not possible to prepare samples of $Ba_{0.3}Sr_{0.7}TcO_3$ and $Ba_{0.4}Sr_{0.6}TcO_3$ in sufficient quantities for NPD measurements, NPD data were collected only for

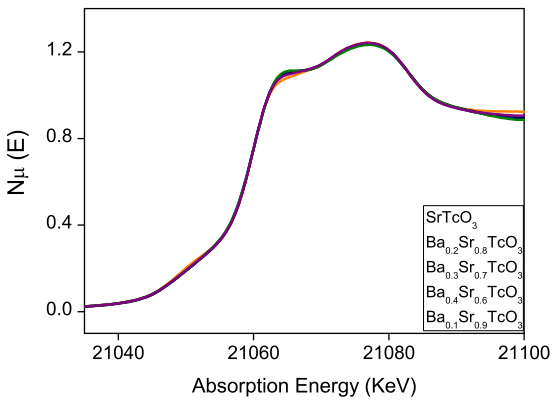

FIG. 2. Normalized Tc K-edge XANES spectra collected from various Ba-doped $Sr_{1-x}Ba_xTcO_3$ samples at room temperature.

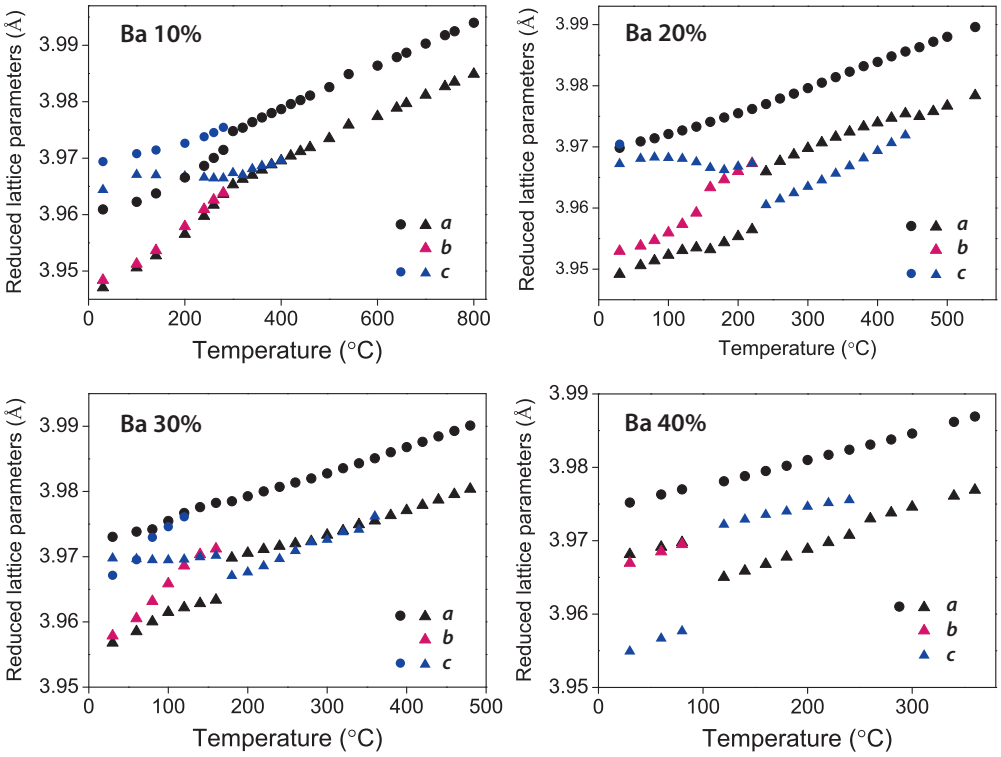

FIG. 3. Temperature dependence of lattice parameters of $Ba_xSr_{1-x}TcO_3$ ($x = 0.1, 0.2$) estimated from Rietveld analysis of synchrotron XRD data. The triangle and circle markers correspond to the Sr- and Ba-rich phase (relative to the ideal composition) for each sample.

the samples with the lowest Ba content, $Ba_{0.1}Sr_{0.9}TcO_3$ and $Ba_{0.2}Sr_{0.8}TcO_3$. In addition the mixed Ca-Sr oxide $Ca_{0.5}Sr_{0.5}TcO_3$ was also studied by NPD between room temperature and 900 °C. These data are compared here with the results obtained previously for $SrTcO_3$ [4]. Examination of the room-temperature NPD patterns of these four samples revealed appreciable intensity in the orthorhombic (110) reflection near $2\theta = 20°$ ($d = 4.57$ Å) as a consequence of magnetic ordering (examples of the refinements shown in Figs. 4 and 5). That only one strong magnetic peak is observed reflects the rapid decrease in intensity with increasing 2θ for $4d$ and $5d$ electrons, due to their delocalized nature [29]. The magnetic contribution to the NPD data was fitted using a G-type AFM magnetic structure, as established previously for $SrTcO_3$ and $CaTcO_3$ [4,10]. In this arrangement, the spin on each cation is aligned antiparallel to those on all six of its nearest neighbors. Phase separation was not apparent in the NPD patterns of the two Ba-containing oxides, presumably due to the lower-peak-shape resolution of the NPD. Consequently the structures were refined against combined SXRD and NPD data sets. The model included two nuclear phases, corresponding to the Ba-rich and Sr-rich compositions described above, and a corresponding magnetic cell. Since the magnetic structure was found to be independent of crystal structure in $SrTcO_3$ [6], the same magnetic structure was used for both compositions. Phase separation was not observed in the SXRD profile for $Ca_{0.5}Sr_{0.5}TcO_3$ and consequently the crystal and magnetic structure of this was refined using NPD data alone.

The paucity and overlap of magnetic reflections in the NPD pattern precluded unconstrained refinement of the two magnetic structures in the Ba-doped oxides. Since the magnetic moments for Tc are essentially the same in $SrTcO_3$ (1.69 μ_β) and $CaTcO_3$ (1.87 μ_β) [4,10] and are the same in the tetragonal and orthorhombic structures of $SrTcO_3$ [6], the Tc magnetic moments in the two phases were constrained to be equal.

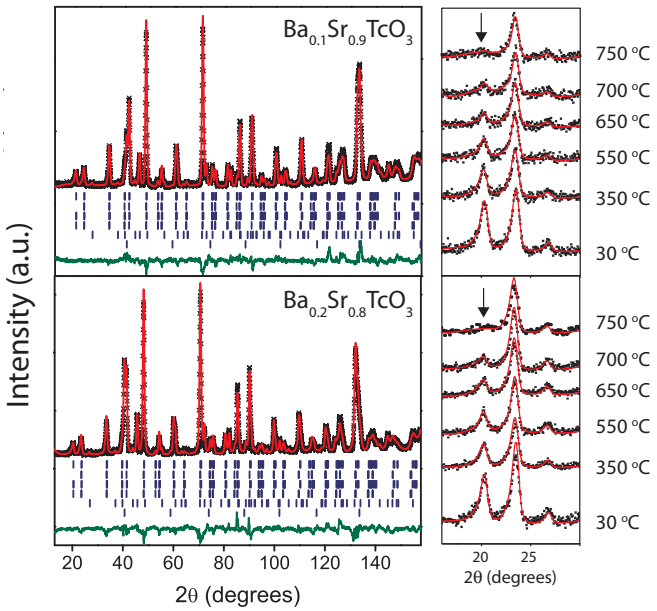

FIG. 4. Left panels show room-temperature NPD ($\lambda = 1.622$ Å) patterns with Rietveld refinement fits to $Ba_{0.1}Sr_{0.9}TcO_3$ and $Ba_{0.2}Sr_{0.8}TcO_3$. Right panels show the temperature dependence of the overlapping (110) and (001) magnetic peaks (indicated by the arrows).

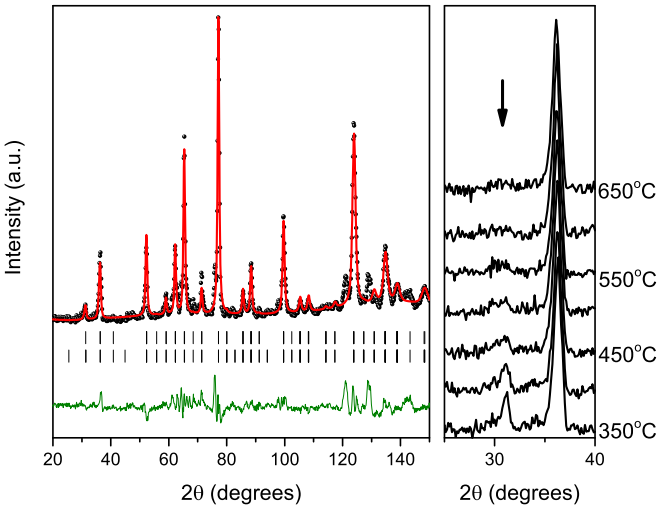

FIG. 5. Left panels show room-temperature NPD ($\lambda = 2.4395$ Å) patterns with Rietveld refinement fits to $Ca_{0.5}Sr_{0.5}TcO_3$. Right panels show the temperature dependence of the (110) + (001) magnetic peaks (indicated by the arrow). The unfitted peaks near 120° are from the furnace.

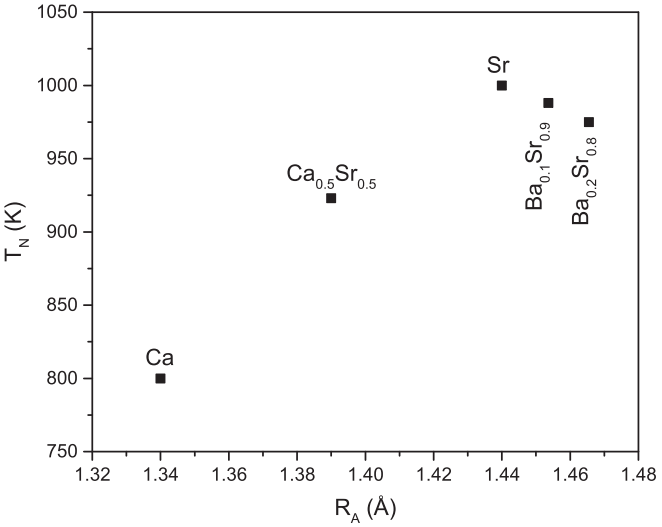

FIG. 7. Variation in the Néel temperatures estimated from neutron diffraction patterns as a function of average A-site ionic radius for the $ATcO_3$. This figure should be compared with the published behavior of $AMnO_3$ [31] and $ARuO_3$ [30] and illustrates that doping $SrTcO_3$ with either Ca or Ba lowers the Néel temperature.

This assumption is further supported by the observation that the incorporation of Ba in $Sr_{1-33x}Ba_xRuO_3$ did not change the magnetization [30]. The refined Tc moments at room temperature of $Ba_{0.1}Sr_{0.9}TcO_3$ and $Ba_{0.2}Sr_{0.8}TcO_3$ are 2.32(14) μ_β and 2.11(13) μ_β, respectively. For $Ca_{0.5}Sr_{0.5}TcO_3$ the refined moment was 1.91(9) μ_β. If it was assumed that only one of the two coexisting phases was magnetic then the refined magnetic moments were unacceptably high. The temperature dependence of the intensity of the magnetic peak for the two Ba-containing oxides is shown in Fig. 4, while the thermal evolution of the refined magnetic moment is given in Fig. 6. The Néel temperatures, estimated by fitting the temperature dependence of the magnetic moments to a function of the type $A(1 - T/T_N)^\beta$, are 714 °C and 702 °C for $Ba_{0.1}Sr_{0.9}TcO_3$ and

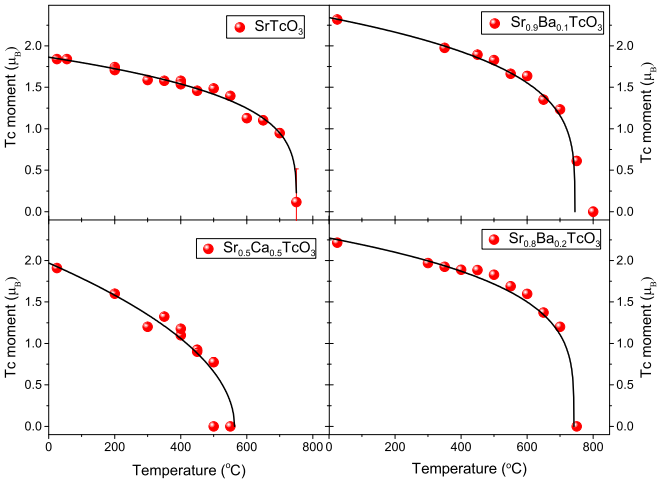

FIG. 6. Temperature dependence of Tc magnetic moments for $Sr_{1-x}A_xTcO_3$ oxides as obtained from Rietveld refinements of NPD data. The solid lines serve as a guide to the eye and are calculated by the function $A(1 - T/T_N)^\beta$ to estimate T_N.

$Ba_{0.2}Sr_{0.8}TcO_3$, respectively. These compare to 550 °C and 750 °C for $Ca_{0.5}Sr_{0.5}TcO_3$ and $SrTcO_3$, respectively.

III. DISCUSSION

In contrast to expectations, the Néel temperature in the series $Sr_{1-x}A_xTcO_3$ ($x = 0.1, 0.2$) decreases with increasing Ba content. The variation of T_N on the effective ionic radius of the A-site cation (R_A) illustrated in Fig. 7 is similar to that observed in the related series $ARuO_3$ [30] and $AMnO_3$ [31] and suggests the maximum magnetic ordering temperature is obtained for $A = Sr$ ($R_A = 1.44$ Å). Furthermore, it appears for the three series that the substitution of Sr by Ca has a more dramatic impact on T_N than doping with Ba. For the Tc system, the Néel temperatures illustrated in Fig. 7 represent the compositions with lowest Ba content in each sample. In drawing this figure we have estimated R_A to correspond to the value for the Sr-rich phase, based on the Rietveld refinements, on the assumption that T_N decreases with Ba content, as observed in the $AMnO_3$ oxides. Consequently the Sr-rich phases will have the higher T_N, and it is this that is estimated from the temperature dependence of the neutron diffraction patterns.

The SXRD patterns demonstrate that each of the $Sr_{1-x}Ba_xTcO_3$ ($x = 0, 0.1, 0.2$) samples transform to the ideal cubic perovskite structure well below T_N. This demonstrates that the composition dependence of the Néel temperature is not simply a consequence of geometric changes as described by the Goodenough-Kanamori rules. To understand this, it is illustrative to compare the isoelectronic Mn and Tc oxides. In the $AMnO_3$ and $ATcO_3$ series, the B-site cations are tetravalent and the electron configuration is $(t_{2g})^3(e_g)^0$. Both $CaTcO_3$ and $CaMnO_3$ [32] adopt an orthorhombic *Pbnm* structure and display G-type AFM ordering. It is reasonable to conclude that the difference in Néel temperature between the two, 800 K in $CaTcO_3$ and 200 K in $CaMnO_3$ [31], is a

consequence of the larger extent of the 4*d* orbitals, relative to the 3*d* orbitals, that enhances the Tc-O orbital overlap, which increases covalency of the Tc-O bond. In both systems, the increase in the Néel temperature upon replacement of the Ca with Sr is ascribed to an increase in the *M*-O-*M* bond angle which strengthens the magnetic exchange interaction and results in an increase in T_N [1,4,6,11,17]. This reasoning, however, does not explain the impact of Ba doping on the behavior of the T_N since these oxides become cubic at temperatures below T_N. Consequently the *M*-O-*M* bond angle is independent of Ba content near the Néel temperature. To explain this, we consider the related Ru ($4d^4$) perovskites. Previous studies have noted similar behavior to that seen here for the Tc oxides in cubic members of the series $Sr_{1-x}Ba_xRuO_3$ [30], where it was suggested that Ba doping impacts the bandwidth through two opposite effects. Firstly because the *A*-O interaction competes with the Ru^{4+} ions for the O-2$p(\pi)$ electrons, the stronger ionic character of the Ba^{2+}, relative to Sr^{2+}, makes it less competitive for the O-2*p* orbitals, which enhances the covalent admixture of O-2$p(\pi)$ character into the primarily 4*d*-electron π^* bands. This broadens the bandwidth *W*. Alternatively, in the cubic structure Ba doping increases the unit cell parameter and hence Ru-O bond length, reducing the bandwidth. Variable pressure studies of $Sr_{1-x}Ba_xRuO_3$ demonstrate the former effect dominates with the increase in the Ru-O bond lengths only partially compensating for the broadening of the Rd 4*d* bands due to the strong ionic character of the Ba^{2+} cation [30]. It appears that the same effect is occurring in the present series, although variable pressure measurements of doped $SrTcO_3$ samples would be required to verify this. These would be extremely technically challenging, given the high Néel temperatures and radioactive nature of the samples.

In summary, polycrystalline samples of $Sr_{1-x}Ba_xTcO_3$ with ideal compositions $x = 0.1, 0.2, 0.3, 0.4$, together with a sample of $Sr_{0.5}Ca_{0.5}TcO_3$ were prepared. Tc *K*-edge XAS measurements have established that the Tc is tetravalent in all cases. SXRD measurements have demonstrated that the Ba-doped samples are poised near a discontinuous *Imma*-$I4/mcm$ transformation and that small variations in composition result in phase separation similar to that seen in other perovskite systems including $Sr_{1-x}Pr_xMnO_3$ [26] and $BaPb_{1-x}Bi_xO_3$ [27]. Using variable temperature neutron powder diffraction it was demonstrated that, contrary to predictions, the Néel temperature decreases with both Ba and Ca content. The behavior of T_N in the $ATcO_3$ system mimics that observed recently in $AMnO_3$ and $ARuO_3$, but with the exception of $CaTcO_3$ the compounds are all cubic at the Néel temperature. This unequivocally demonstrates the importance of the broadening of the π^* bandwidth *W* by the *A*-site cation. It is hoped that these experimental studies will inspire additional efforts to quantify the relative effects of covalency and local bond distance changes in tuning magnetic interactions in the heavier transition-metal oxides.

ACKNOWLEDGMENTS

We acknowledge the assistance of Terry McLeod and Mike Jovanovic in sample preparation at ANSTO. The authors thank Mr. Trevor Low and Ms. Julie Bertoia for health physics support at UNLV. B.J.K. acknowledges the support of the Australian Research Council. F.P. acknowledges the Department of Chemistry and Biochemistry at UNLV for supporting his research through a startup package. This work was, in part, performed at the powder diffraction and x-ray spectroscopy beamlines at the Australian Synchrotron.

[1] C. L. Ma, Y. Zhu, T. C. Zang, and X. D. Wang, Phys. Lett. A **375**, 3615 (2011).
[2] S. Middey, A. K. Nandy, S. K. Pandey, P. Mahadevan, and D. D. Sarma, Phys. Rev. B **86**, 104406 (2012).
[3] J. Mravlje, M. Aichhorn, and A. Georges, Phys. Rev. Lett. **108**, 197202 (2012).
[4] E. E. Rodriguez, F. Poineau, A. Llobet, B. J. Kennedy, M. Avdeev, G. J. Thorogood, M. L. Carter, R. Seshadri, D. J. Singh, and A. K. Cheetham, Phys. Rev. Lett. **106**, 067201 (2011).
[5] T. Takeda and S. Ohara, J Phys. Soc. Jpn. **37**, 275 (1974).
[6] G. J. Thorogood, M. Avdeev, M. L. Carter, B. J. Kennedy, J. Ting, and K. S. Wallwork, Dalton Trans. **40**, 7228 (2011).
[7] J. M. Longo, P. M. Raccah, and J. B. Goodenough, J. Appl. Phys. **39**, 1327 (1968).
[8] I. I. Mazin and D. J. Singh, Phys. Rev. B **56**, 2556 (1997).
[9] S. Calder, V. O. Garlea, D. F. McMorrow, M. D. Lumsden, M. B. Stone, J. C. Lang, J.-W. Kim, J. A. Schlueter, Y. G. Shi, K. Yamaura, Y. S. Sun, Y. Tsujimoto, and A. D. Christianson, Phys. Rev. Lett. **108**, 257209 (2012).
[10] M. Avdeev, G. J. Thorogood, M. L. Carter, B. J. Kennedy, J. Ting, D. J. Singh, and K. S. Wallwork, J. Am. Chem. Soc. **133**, 1654 (2011).
[11] C. Franchini, T. Archer, J. He, X.-Q. Chen, A. Filippetti, and S. Sanvito, Phys. Rev. B **83**, 220402(R) (2011).
[12] C. M. Dai and C. L. Ma, Mod. Phys. Lett. B **28**, 1450049 (2014).
[13] C. L. Ma, C. M. Dai, G. Y. Chen, D. Chen, T. C. Zang, L. J. Ge, W. Zhou, and Y. Zhu, Solid State Commun. **219**, 25 (2015).
[14] C. L. Ma and T. Zhou, Physica B **407**, 218 (2012).
[15] G. T. Wang, L. Li, C. Liu, M. P. Zhang, and Z. X. Yang, Phys. Lett. A **376**, 3313 (2012).
[16] W. Zhang and P. Q. Tong, J. Phys.: Condens. Matter **24**, 185401 (2012).
[17] V. S. Borisov, I. V. Maznichenko, D. Böttcher, S. Ostanin, A. Ernst, J. Henk, and I. Mertig, Phys. Rev. B **85**, 134410 (2012).
[18] Y. Syono, S. I. Akimoto, and K. Kohn, J. Phys. Soc. Jpn. **26**, 993 (1969).
[19] O. Muller, W. B. White, and R. Roy, J. Inorg. Nucl. Chem. **26**, 2075 (1964).
[20] See Supplemental Material at http://link.aps.org/supplemental/10.1103/PhysRevB.95.054430 for additional XRD profiles and crystallographic parameters.
[21] K. S. Wallwork, B. J. Kennedy, and D. Wang, AIP Conf. Proc. **879**, 879 (2007).
[22] K. D. Liss, B. Hunter, M. Hagen, T. Noakes, and S. Kennedy, Physica B **385-386**, 1010 (2006).
[23] C. Glover, J. McKinlay, M. Clift, B. Barg, J. Boldeman, M. Ridgway, G. Foran, R. Garrett, P. Lay, and A. Broadbent, AIP Conf. Proc. **882**, 884 (2007).

[24] C. J. Howard, K. S. Knight, B. J. Kennedy, and E. H. Kisi, J. Phys.: Condens. Matter **12**, L677 (2000).
[25] B. J. Kennedy, B. A. Hunter, and J. R. Hester, Phys. Rev. B **65**, 224103 (2002).
[26] T. Y. Tan, N. Martin, Q. D. Zhou, B. J. Kennedy, Q. F. Gu, J. A. Kimpton, Z. M. Zhang, and L. Y. Jang, J. Solid State Chem. **201**, 115 (2013).
[27] E. Climent-Pascual, N. Ni, S. Jia, Q. Huang, and R. J. Cava, Phys. Rev. B **83**, 174512 (2011).
[28] B. J. Kennedy, M. Avdeev, H. L. Feng, and K. Yamaura, J. Solid State Chem. **237**, 27 (2016).
[29] S. N. Bushmeleva, V. Y. Pomjakushin, E. V. Pomjakushina, D. V. Sheptyakov, and A. M. Balagurov, J. Magn. Magn. Mater. **305**, 491 (2006).
[30] C. Q. Jin, J. S. Zhou, J. B. Goodenough, Q. Q. Liu, J. G. Zhao, L. X. Yang, Y. Yu, R. C. Yu, T. Katsura, A. Shatskiy, and E. Ito, Proc. Natl. Acad. Sci. USA **105**, 7115 (2008).
[31] O. Chmaissem, B. Dabrowski, S. Kolesnik, J. Mais, D. E. Brown, R. Kruk, P. Prior, B. Pyles, and J. D. Jorgensen, Phys. Rev. B **64**, 134412 (2001).
[32] Q. D. Zhou and B. J. Kennedy, J. Phys. Chem. Solids **67**, 1595 (2006).